Colloids and Surfaces A: Physicochem. Eng. Aspects 322 (2008) 199–210

Contents lists available at ScienceDirect

Colloids and Surfaces A: Physicochemical and Engineering Aspects

journal homepage: www.elsevier.com/locate/colsurfa

Rheology of colloidal gas aphrons (microfoams)

Sophie Larmignat, Damien Vanderpool, Heung Kei Lai, Laurent Pilon*

University of California, Los Angeles, Mechanical and Aerospace Engineering Department, 420 Westwood Plaza, Los Angeles, CA 90095-1597, United States

ARTICLE INFO

Article history:
Received 21 November 2007
Received in revised form 25 February 2008
Accepted 6 March 2008
Available online 15 March 2008

Keywords:
Microfoams
Remediation
Separation
Bioreactors
Oil recovery
Aqueous foam
Foam rheology
Pipe flow

ABSTRACT

This paper reports on the effect of surfactant concentration and pipe shape and size on the rheological properties of colloidal gas aphrons (CGAs) or microfoams. CGA consists of closely packed spherical gas bubbles with diameter ranging from 10 to 100 μm surrounded by a surfactant shell. It is produced by stirring an aqueous surfactant solution at high speed in a baffled beaker. Pipe flow experiments were performed in cylindrical pipes with diameter ranging from 1.0 to 3.0 mm under adiabatic laminar flow conditions. The porosity, bubble size distribution, surface tension, and pH were systematically measured. First, it is established that there was no slip velocity at the wall and CGA did not change morphology and porosity between the inlet and outlet of the pipes less than 2 mm in diameter. Compressibility effects were accounted for through the volume equalization approach. Then, pipe shape and diameter have no effect on the CGA rheology. Finally, CGA can be considered as a shear-thinning fluid. The dimensionless volume equalized shear stress τ^* is proportional to $(Ca^*)^m$ where Ca^* is the Capillary number and $m = 0.65 \pm 0.06$. The results are in good agreement with theoretical models suggesting $\tau^* = C(x)(Ca^*)^{2/3}$ where $C(x)$ is determined experimentally. It is established that $C(x)$ increases with surfactant mass fraction x. The Fanning friction factor f for CGA under laminar flow conditions follows the standard relationship $f = 16/Re_D$ where Reynolds number is determined using the CGA effective viscosity given by $\mu_e = \mu_l C(x) Ca^{-1/3}$.

1. Introduction

Colloidal gas aphrons (CGAs), also called microfoams, consist of closely packed spherical bubbles between 10 and 100 μm in diameter and porosity around 0.7 [1]. They are produced by stirring an aqueous surfactant solution contained in a fully baffled beaker via a spinning disk driven at high speed by an electric motor [1].

Colloidal gas aphrons have found numerous applications including (1) protein or bacteria separation [2,3], (2) soil remediation [4,5], (3) remediation of contaminated water [6,7], (4) fermentation and bioreactors [8], and (5) material synthesis [9–11]. These applications take advantage of (i) their large interfacial area, (ii) the adsorption of particles at the microbubble interfaces, and (iii) their stability for enhanced mass transfer [12]. They could also be used in oil recovery and fire fighting. In most of these applications, CGA is pumped through columns, pipes, and fittings. Thus, it is of practical interest to investigate the rheology of CGA to enable optimum process design. It is also of fundamental interest in the field of soft-matter physics where aqueous foams have been a subject of intense studies. There, the objectives are to model and measure the foam morphology and the different physical phenomena taking place in foams as well as to predict their effect on the mechanical and rheological properties [13,14].

Colloidal gas aphrons differ from regular foams in terms of bubble morphology. Foams consist of gas bubbles covered by a monolayer of surfactant molecules immersed in the solution which may contain micelles. On the other hand, the most widely accepted structure of CGA bubbles, suggested by Sebba [1], speculates that bubbles are encapsulated in a multilayered shell consisting of surfactant and liquid. The main supporting arguments were (i) the absence of bubble coalescence, (ii) the fact that hydrophobic globules attach to the surface of the bubbles, and (iii) that when the CGA is created in dyed water and the generated bubbles are transferred into clear water, the bubbles contained some dyed water in their shell. Finally, Sebba [1] did not elaborate on the thickness of the speculative soapy shell. Amiri and Woodburn [16] estimated the thickness of the soapy shell to be 750 nm for cationic surfactant CTAB. They studied the liquid drainage rate in CGA dispersion and the bubble rise velocity. Bredwell and Worden [12] estimated the shell thickness to be 200–300 nm for non-ionic surfactant Tween 20, based on the study of gas diffusion from the CGA bubble to the liquid bulk, assuming that the mass transfer is limited by the rate of diffusion across the shell. More recently, Jauregi et al. [15] employed freeze fracture with TEM and X-ray diffraction to study the structure of the soapy shell. They imaged and measured the thickness of a surfactant shell to be 96 nm. They argued that the shell does

* Corresponding author. Tel.: +1 310 206 5598; fax: +1 310 206 2302.
E-mail address: pilon@seas.ucla.edu (L. Pilon).

0927-7757/$ – see front matter © 2008 Elsevier B.V. All rights reserved.
doi:10.1016/j.colsurfa.2008.03.010

Nomenclature

a	parameter for minor losses, Eq. (12)
$B(x)$	empirical function in $\tau^* = B(x)(Ca^*)^m$, Eq. (18)
$C(x)$	empirical function in $\tau^* = C(x)(Ca^*)^{2/3}$, Eq. (19)
Ca	Capillary number, $Ca = \mu_l r_{32}\dot{\gamma}_a/\sigma$
Ca^*	volume equalized Capillary number, $Ca^* = \mu_l r_{32}\dot{\gamma}_a/\varepsilon\sigma$
d	bubble diameter (m)
D_h	hydraulic diameter based on the wetted perimeter (m)
D_i	Lexan rod inner diameter (m)
K_B, K_{HB}, K_P, K_{VE}	flow consistency for various models
K_{L1}, K_{L2}	minor loss coefficients
L	distance between pressure sensors (m)
L_e	entry length (m)
m	empirical constant in $\tau^* = B(x)(Ca^*)^m$
$\dot{m}$	mass flow rate (kg/s)
M	mass (kg)
n, n', n''	flow behavior indices
ΔP	pressure drop (Pa)
$\dot{Q}$	volumetric flow rate (m^3/s)
r_{32}	Sauter mean bubble radius (m)
Re_D	Reynolds number
t	time (s)
u_f	average fluid velocity in a channel (m/s)
u_s	wall slip velocity (m/s)
V	volume (m^3)
x	surfactant mass fraction (wt.%)

Greek symbols

α	empirical constant, $u_s = \alpha\tau_w$
β	empirical constant, Eq. (9)
$\dot{\gamma}_a$	apparent shear rate (s^{-1})
$\dot{\gamma}_{a\text{-}s}$	apparent shear rate corrected for slip velocity (s^{-1})
$\dot{\gamma}_w$	true wall shear rate (s^{-1})
ε	specific expansion ratio, ρ_l/ρ_{CGA}
μ	dynamic viscosity (Pa s)
ρ	density (kg/m^3)
σ	surface tension (N/m)
τ_w	wall shear stress (Pa)
τ_0	yield shear stress (Pa)
ϕ	volume fraction of air in CGA or porosity, V_g/V_{CGA}

Subscripts

CGA	refers to CGA
e	effective property
exp	refers to measured data
f	refers to working fluid in general (water or CGA)
g	refers to gas in CGA
l	refers to the liquid-phase or single-phase water
w	refers to the wall

not provide room for finite inner water phase as proposed by Sebba [1]. Thanks to X-ray diffraction, they showed that the soapy shell consisted of more than one layer of surfactant molecules. However, they noticed a large uncertainty on the exact number of layers. It remains unclear, however, if and how rheological properties of CGA differ from that of foams.

The present study aims at experimentally investigating the rheology of CGA flowing in cylindrical pipes with various diameters and different concentrations of the non-ionic surfactant Tween 20. It also compares the experimental results with theoretical models proposed in the literature for regular foams.

2. Background

2.1. Foam rheology

Liquid foams are known to be non-Newtonian fluids. Different rheological models have been proposed to predict the evolution of the wall shear stress τ_w as a function of the apparent shear rate $\dot{\gamma}_a$ [14,17,18]. In brief, the pseudo-plastic power-law model has been widely used [19–24] after correcting for possible wall slip velocity. Then, the wall shear stress τ_w, the true wall shear rate $\dot{\gamma}_w$, and the apparent shear rate $\dot{\gamma}_a$ are related by the power law:

$$\tau_w = K_P\dot{\gamma}_w^n = K_P'\dot{\gamma}_a^n = \mu_e\dot{\gamma}_a \quad (1)$$

where K_P and n are the so-called flow consistency and flow behavior, respectively. The apparent shear rate $\dot{\gamma}_a$ corresponds to what the wall shear rate would be if the fluid were Newtonian. The true wall shear rate $\dot{\gamma}_w$ can be derived from $\dot{\gamma}_a$ through the Rabinowitsch–Mooney relationship [25]:

$$\dot{\gamma}_w = \left(\frac{3n+1}{4}\right)\dot{\gamma}_a \quad \text{and} \quad K_P' = K_P\left[\frac{3n+1}{4n}\right]^n \quad (2)$$

On the other hand, Khan et al. [26] found experimentally that polymer–surfactant-based aqueous foams with porosity larger than 0.9 and bubble diameter around 65 μm behave as a Bingham fluid for which the shear stress is expressed as

$$\tau_w = \tau_0 + K_B\dot{\gamma}_w \quad (3)$$

where τ_0 is the yield stress and K_B is an empirical constant.

The Herschel–Bulkley model encompasses the previous models. It has been used successfully for macrofoams made of aqueous polymer solutions [14,27] and is given by

$$\tau_w = \tau_0 + K_{HB}\dot{\gamma}_w^{n'} \quad (4)$$

where τ_0 is the yield stress, K_{HB} is the consistency, and n' is the power-law index.

The above models are typically used for incompressible fluids. However, foams and CGA are compressible fluids which can be analyzed using the volume equalization method proposed by Economides and co-workers [19–21] and successfully applied to flow of polymer foams under high pressure. Their model relates the volume equalized shear stress to the volume equalized shear rate according to the power law:

$$\frac{\tau_w}{\varepsilon} = K_{VE}\left(\frac{\dot{\gamma}_w}{\varepsilon}\right)^{n''} \quad (5)$$

where K_{VE} and n'' are empirical constant while ε is the specific expansion ratio defined as the ratio of the densities of the liquid phase and foams or CGA, i.e., $\varepsilon = \rho_l/\rho_{CGA} = 1/(1-\phi)$ where ϕ is the gas volume fraction or porosity.

Moreover, mechanistic models have been developed to overcome the limitations of empirical correlations in predicting the rheology of foams made from surfactant solutions different from those for which they were developed. Earlier models considered two-dimensional foams with large gas volume fraction (porosity) and perfectly ordered and monodispersed bubbles. First, Khan and Armstrong [28] and Kraynick and Hansen [29] focused on the liquid film separating the bubbles as the source of viscous dissipation. Based on their model, they concluded that foams behave as a Bingham fluid (Eq. (1)). This result was confirmed experimentally by Khan et al. [26] but contradicts numerous other experimental evidences for both foams [19–24] and emulsions [30].

Alternatively, Schwartz and Princen [31] focused on the Plateau border where the liquid was assumed to be confined. The authors expanded Bretherton's model [32] for pressure drop along a single bubble flowing in capillary tubes. They solved the Navier–Stokes

equations under lubrication approximation with immobile interfaces due to the presence of surfactants. Assumptions also suggest that the liquid separating the bubble is inherently thick [33]. The resulting model predicts that the shear stress is expressed as [30]:

$$\tau_w = \tau_0 + C(\phi)\frac{\sigma}{r_{32}}Ca^{2/3} \quad (6)$$

where τ_0 is the yield stress, r_{32} is the Sauter mean bubble/drops radius, and σ is the surface tension of the gas/liquid interface. The Capillary number Ca represents the ratio of the viscous to the surface tension forces and is defined as

$$Ca = \frac{\mu_l r_{32}\dot{\gamma}_a}{\sigma} \quad (7)$$

where μ_l is the viscosity of the liquid phase. Cantat and co-workers [36,37] studied a two-dimensional train of bubbles consisting of one to three layers of 20–50 individual monodispersed bubbles, a few millimeters in diameter, flowing in small channels of rectangular cross-section. Their results extend Bretherton's model [32] for a train of bubbles to foam and showed that the pressure drop along the bubble chain was proportional to $Ca^{2/3}$ [36]. In Ref. [37] the authors found that the viscous force per unit length of Plateau border was proportional to $Ca^{0.56}$ which was judged to be in "fair agreement with the theoretical prediction" suggesting $Ca^{2/3}$. However, individual bubbles were the same size as the pipe diameter and foam could not be treated as an effective fluid. On the other hand, experiments with oil/water emulsions [30] for oil volume fraction larger than 0.8 indicated that the power 1/2 fitted the data better than 2/3.

These discrepancies were recently attributed to the surface mobility of the bubbles [34,35]. Indeed, Denkov et al. [34,35] suggested that Schwartz and Princen's model [31] was not applicable to continuous shear flow. They also used a similar approach to that of Bretherton [32] but accounted for the viscous friction over the entire area separating the bubbles from the wall as opposed to considering only the front and rear of the bubbles as done by Bretherton [32]. They concluded that the shear stress is proportional to $Ca^{2/3}$ for tangentially *mobile* bubble surface and to $Ca^{1/2}$ for tangentially *immobile* surface. Surface mobility depends on various parameters including the surface dilatational modulus whose large value ensures tangentially immobile surface. Their model was confirmed experimentally for aqueous foams with porosity of 0.9 made from various surfactant solutions with a wide range of surface dilatational modulus [34].

Furthermore, Durian [38,39] described two-dimensional foams as an ensemble of closely packed polydisperse and randomly distributed hard spheres. He performed molecular dynamics simulations on the system accounting for surface tension, viscous drag, compression from neighboring bubbles, and external shear rate. His model was extended to three-dimensional foams by Gardiner et al. [40]. Both 2D and 3D studies conclude that the foam behaves as a Bingham fluid represented by Eq. (3).

Experimentally, care should be taken to isolate the rheological properties of CGA or foams from transient phenomena such as liquid drainage and bubble coalescence. To do so, rheological measurement systems should meet the following requirements [17,18]: (1) the foam should remain unchanged throughout the duration of the measurements, (2) the porosity and bubble size distribution should be measured, (3) the surface tension of the solution/air system should be known, (4) the wall slip velocity should be accounted for whenever observed [17,18], and (5) the absolute operating pressure and temperature should be reported as they both affect the porosity, bubble size distribution, and properties of both phases. Note that many experimental foam rheology studies did not report the porosity [41], the bubble size distribution [42], and/or the surface tension of the liquid/air system [20,42–44]. Measurements using rotational viscometers [26] consist of subjecting the foams to shearing until "a steady state" torque can be measured. However, "reproducibility of data as well as steady-state measurements have been difficult to achieve in practice" [17]. Alternatively, flow pipe viscometers have been considered by various authors for macrofoams [14,19–21] and for CGA [45]. Detailed reviews of pipe flow experiments used to determine the rheology of aqueous foams have been summarized elsewhere [14,17,18,43]. Foams or CGA are treated as a pseudo-homogeneous time-independent non-Newtonian fluid. This requires that the pipe diameter be much larger (10–20 times) than the bubble size [17,46]. The wall shear stress τ_w and the apparent shear rate $\dot{\gamma}_a$ are experimentally determined from the pressure drop ΔP and the volumetric flow rate $\dot{Q}$ according to [19,20]:

$$\tau_w = \frac{D_h \Delta P}{4L} \quad \text{and} \quad \dot{\gamma}_a = \frac{32\dot{Q}}{\pi D_h^3} \quad (8)$$

where D_h is the hydraulic diameter of the pipe and ΔP is the pressure drop between the pressure sensors separated by a distance L.

2.2. Wall slip velocity

As previously discussed, a slip velocity may exist at the wall due to the presence of a thin liquid film. For example, Thondavali and Lemlich [23] found that slip velocity is significant in foam flowing in acrylic pipes while it vanishes for stainless steel pipes with diameter 1–5 cm. Similarly, no slip velocity was measured by Harris and Reidenbach [47] on foam flowing in stainless steel pipes.

Moreover, the wall slip velocity can be reduced or eliminated by making the wall surface rough so that the liquid film can fill the surface depressions [26]. Several methods have been proposed to recover the slip velocity from pipe flow experiments. First, Mooney [48] assumed that the slip velocity u_s was proportional to the shear stress τ_w, i.e., $u_s = \alpha\tau_w$ where α is an empirical constant. However, several studies have established that this assumption does not apply to foams [17,19–21,27]. The most suitable method was proposed by Oldroyd [49] and Jastrzebski [50] who suggested that the wall slip velocity is proportional to the shear stress and inversely proportional to the pipe diameter. It has been used successfully to analyze pipe flow experiments with aqueous foams [20,27]. Then, the wall slip velocity is estimated by

$$\dot{\gamma}_a = \dot{\gamma}_{a\text{-}s} + \frac{8u_s}{D_h} \quad \text{with } u_s = \beta\frac{\tau_w}{D_h} \quad (9)$$

where β is an empirical constant depending on τ_w and determined from the slope of $\dot{\gamma}_a$ plotted as a function of $1/D_h^2$ for different values of τ_w. The apparent shear rate corrected for slip $\dot{\gamma}_{a\text{-}s}$ corresponds to the nominal shear rate depending only on the wall shear stress and independent of the pipe diameter [20].

The present study differs from previous ones in that it considers CGA or microfoams consisting of numerous randomly distributed polydisperse micron size bubbles forming a three-dimensional structure with a relatively small porosity ϕ ranging from 0.63 to 0.72. Pipe flow experiments are performed to ensure that the foam morphology does not change during the course of the measurements.

3. Experiment

3.1. Experimental setup

First, CGA was generated by continuously stirring an non-ionic aqueous surfactant solution with a Silverson L4RT mixer at

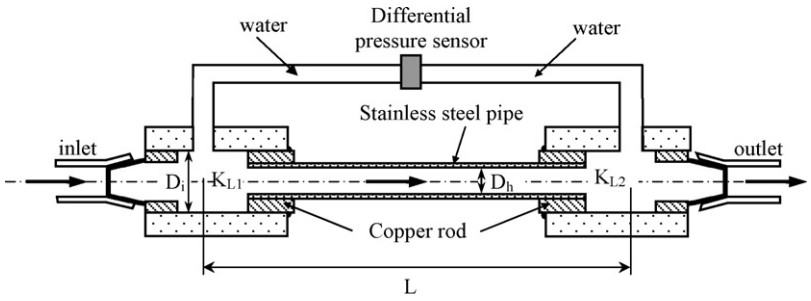

Fig. 1. Schematic of the test section showing minor losses and pressure sensor.

7000 rpm in a baffled container [1]. The solution was made from an arbitrary mass fraction x of polyoxyethylene sorbitan monolaurate (Tween 20) by USB Corp. (USA) in deionized water. The container was placed in a large tank filled with water and acting as a thermal reservoir to maintain the CGA at constant temperature. Type T thermocouples were placed in the CGA container as well as the water reservoir and connected to the data acquisition system. The CGA was continuously produced and flown through the test section. This ensured that CGA kept the same morphology and porosity as it traveled through the test section as verified experimentally [45].

The experimental setup was that of a typical pipe flow experiment consisting of (i) a supply tank, (ii) a volumetric pump, (iii) a data acquisition system connected to a personal computer, and (iv) a test section shown in Fig. 1. The different test sections consisted of stainless steel 304 pipes with diameter D_h and tightly fitted through a copper rod. Sealing was achieved by soldering the steel pipe and the copper rods which were then screwed in Lexan® rods. The test section was supported by a G10 slab placed above and underneath the pipe to ensure that it was straight and horizontal. The Lexan® rods connected the test section to the rest of the experimental setup and hosted the pressure sensor. A differential pressure sensor measured the pressure drop over the distance L to include the viscous losses in the pipe as well as the minor losses due to sudden contraction and expansion at the inlet and outlet of the pipe (Fig. 1). Note that the test section was designed to minimize the overall minor losses and to enable accurate determination of the remaining two minor losses. For the range of pipe diameter and flow rate investigated, the measured pressure drop ΔP_{exp} varied between 0 and 6.89×10^3 Pa (30 psi). The tubing connecting the pressure sensors to the inlet and outlet fixtures was filled with water (incompressible) prior to each series of tests to ensure accurate measurement of the differential pressure.

Data analysis is very sensitive to the value of the pipe diameter. Thus, the inside diameter of each pipe was measured 10 times at both ends with an electronic caliper. The average diameters of the four different pipes were found to be 1.0301 ± 0.0268, 1.4859 ± 0.0240, 2.0155 ± 0.0398, and 2.9959 ± 0.0604 mm with a 95% confidence level. In addition, the length of each pipe was chosen to ensure that (i) accurate measurements of the pressure drop could be obtained with the pressure sensors and (ii) fully developed flow conditions prevailed throughout most of the pipe, i.e., $L \gg L_e$ where the entry length L_e is expressed as $L_e/D_h = 0.06Re_D$ [51]. Thus, the distance L between the differential pressure sensors was equal to (i) 0.338 m for pipe diameters of 1.03, 1.49, and 2.02 mm and (ii) 1.05 m in length for diameter 3.00 mm. Since the length of the test section was relatively small, the pressure gradient was assumed to be constant along the channels, i.e., $dP/dx \approx -\Delta P/L$ [17]. This assumption has also been confirmed in recent experimental studies on foams [52].

3.2. Experimental procedure

The parameters measured experimentally were the pressure drop along the channel ΔP_{exp}, the temperatures of the fluid and of the water reservoir, the volumetric flow rate $\dot{Q}$, and the mass flow rate $\dot{m}$. The volume of CGA, V_{CGA}, exiting the test section was determined by either a graduated Kimax 100 mL cylinder or a Nalgene 1 L beaker while the time t was measured by a stop watch. The volumetric flow rate $\dot{Q}$ was estimated from the slope of $V_{CGA}(t)$ versus time t. The mass flow rate was estimated from the slope of the plot of the mass $M_{CGA}(t)$ of outflowing CGA versus time. The scale used was a compact digital bench scale from Ohaus, model Scout Pro SP401 with range between 0 and 400 g. The reading of the mass $M_{CGA}(t)$ and volume $V_{CGA}(t)$ of outflowing CGA were simultaneously recorded with a video camera. They were then, determined by analyzing the video in slow motion. This process was repeated for different flow rates. Each experiment was allowed to run for a minimum of 3 min so that steady-state conditions were reached. Then, the data acquisition unit was turned on to record the pressure drop ΔP_{exp} and temperatures every second for 10 min. During that time the pressure and temperature readings did not fluctuate significantly and measurements were averaged over time.

The porosity of CGA was then computed from the following definition [45]:

$$\phi(t) \equiv \frac{V_g(t)}{V_{CGA}(t)} \simeq 1 - \frac{M_{CGA}(t)}{\rho_l V_{CGA}(t)} \tag{10}$$

Experimentally, the porosity ranged from 0.6 to 0.75 and varied within 2% over the recording time. It was also established experimentally that porosity varied by less than 2% between the inlet and outlet of all test sections. For all cases, the CGA temperature was $25 \pm 2\,^{\circ}C$ and the reservoir temperature remained constant at $22 \pm 1\,^{\circ}C$. Without the thermal reservoir, the temperature of the CGA would have increased during the measurements. The pipe was thoroughly rinsed with deionized water and dried overnight every day or between two CGA batches. Finally, the surface tension of the air/aqueous surfactant solution system was measured before each batch of CGA using a semi-automatic Cole–Parmer tensiometer employing the du Noüy ring method.

3.3. Pressure drop

For both water and CGA, the minor losses due to sudden contraction and expansion in the test section (Fig. 1) were subtracted from the measured differential pressure ΔP_{exp} in order to derive the differential pressure ΔP due to friction losses along the pipe [51]:

$$\Delta P = \Delta P_{exp} - \tfrac{1}{2}\rho_f u_f^2 (K_{L1} + K_{L2}) \tag{11}$$

where ρ_f is the fluid (water or CGA) density and u_f is the average fluid velocity obtained from the volumetric flow rate measurements. The coefficients K_{L1} and K_{L2} are the minor losses associated with sudden contraction and expansion, respectively. The former is given by [51]:

$$K_{L1} = a\left(1 - \frac{D_h^2}{D_i^2}\right)^2 \quad (12)$$

where the parameter a is equal to 2.0 for laminar flow [51] while D_h is the pipe hydraulic diameter and D_i is the hydraulic diameter of the Lexan rod which is equal to 11.25 mm for all pipes. In addition, K_{L2} was determined graphically from Ref. [51] (p. 350) and found equal to 0.5. Minor losses increased with increasing flow rates. The minor losses represented between (i) 1.5 and 12% of the measured pressure drop ΔP_{exp} for the 1.03 mm pipe, (ii) 0.1 and 16% for the 1.49 mm pipe, (iii) 0.0 and 30% for 2.03 mm pipe, and (iv) 0.08 and 18% for the 3.00 mm pipe. Finally, the absolute operating pressure was about 1 atm for all runs.

3.4. Error analysis

Experimentally, it is impossible to achieve the same porosity for each run and solution. Assuming that the uncertainty associated with the density of water ρ_l is negligible, Eq. (10) suggests that the uncertainty in the measured porosity is expressed as

$$\frac{\Delta\phi}{\phi} = \sqrt{\left(\frac{\Delta\dot{m}}{\dot{m}}\right)^2 + \left(\frac{\Delta\dot{Q}}{\dot{Q}}\right)^2} \quad (13)$$

The uncertainty in the mass flow rate $\dot{m}$ and the volumetric flow rate $\dot{Q}$ was estimated at 5% resulting in an uncertainty $\Delta\phi/\phi$ of about 7%. Consequently, since the porosity of CGA was about 0.7, all tests with porosity between 0.65 and 0.75 were considered in the analysis except for solution 1 containing 0.028 wt.% of Tween 20 whose porosity was 0.63 ± 0.05.

Moreover, the expressions for the fractional uncertainties in τ_w and $\dot{\gamma}_a$ derived from Eq. (1) are

$$\frac{\Delta\tau_w}{\tau_w} = \sqrt{\left(\frac{\Delta D_h}{D_h}\right)^2 + \left(\frac{\Delta L}{L}\right)^2 + \left[\frac{\Delta(\Delta P)}{\Delta P}\right]^2} \quad (14)$$

$$\frac{\Delta\dot{\gamma}_a}{\dot{\gamma}_a} = \sqrt{\left(\frac{\Delta\dot{Q}}{\dot{Q}}\right)^2 + \left(3\frac{\Delta D_h}{D_h}\right)^2} \quad (15)$$

Note that the uncertainty in the apparent shear stress $\dot{\gamma}_a$ is dominated by the error in the measurement of the pipe diameter D_h. The uncertainties $\Delta\tau_w/\tau_w$ and $\Delta\dot{\gamma}_a/\dot{\gamma}_a$ could be large for small flow rates. For all experimental data reported here, $\Delta\tau_w/\tau_w$ was less than 15% and $\Delta\dot{\gamma}_a/\dot{\gamma}_a$ was less than 7%.

4. Results and discussion

4.1. Validation of experimental setup and analysis

The experimental setup, sensors, calibration, and analysis were validated by measuring the viscosity of deionized water and comparing it with values obtained from the thermophysical properties database DIPPR [53]. The average water temperature for measurements in the 1.03, 1.49, 2.02, and 3.0 mm diameter pipes was 22.7, 22.1, 22.1 and 21.8 °C, respectively, while that for the rectangular channel was 25 °C [45]. Fig. 2 shows the shear stress τ_w versus apparent shear rate $\dot{\gamma}_a$ for water at the average temperature of 22.5 ± 1 °C in the five different pipes considered. It indicates that

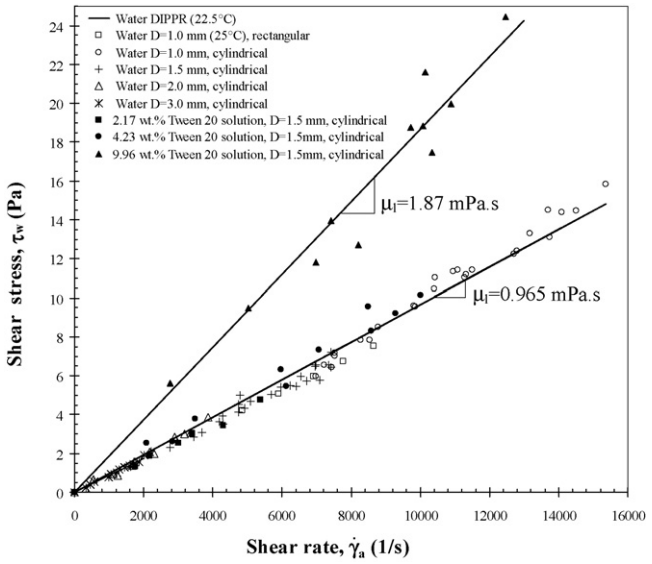

Fig. 2. Shear stress vs. shear rate for deionized water and aqueous solutions of Tween 20 with mass fraction 2.17, 4.23, and 9.96 wt.%.

τ_w is linearly proportional to $\dot{\gamma}_a$ as expected for a Newtonian fluid. The corresponding viscosity of water retrieved from the 1.03, 1.49, 2.02, and 3.0 mm pipe flow experiments was 0.991, 0.885, 0.934, and 0.871 mPa s, respectively. These values fall, respectively, within 2.6, 7.3, 3.2, and 9.7% of the viscosity of water given by the DIPPR database as equal to 0.965 ± 0.022 mPa s at 22.5 ± 1 °C [53]. Given the uncertainty associated with the pressure drop, the pipe diameter, and the mass and volumetric flow rates measurements as well as the minor loss coefficients, these results are considered to be very good.

Finally, in order to validate the surface tension measurements, the surface tension of tap water was measured 10 times and found equal to 71.8 ± 0.6 mN/m with 95% confidence level in good agreement with the literature [54].

4.2. Solution characteristics and CGA morphology

Table 1 summarizes the characteristics of the surfactant solutions used and those of the corresponding CGA. It includes the surfactant mass fraction x, the surface tension σ, the pH, the Sauter mean bubble radius r_{32}, and the average porosity ϕ. All variables were measured before each experimental run and averaged.

Fig. 3 shows the micrographs of CGA formed with aqueous solutions of Tween 20 at different concentrations while Fig. 4 shows the associated bubble size distribution. The latter was measured based on micrographs of CGA observed under a Leica DM IL microscope and sampled from the container less than 1 min after it was generated. The bubble size distribution was measured from 170 to 305 individual bubbles using the image analysis software Image J. The Sauter mean bubble radius r_{32} was between 36 and 48 μm for all solutions. The bubble size distribution was narrower for the largest Tween 20 concentrations. Note that the image analysis was made difficult by optical effects and multilayer close packing of CGA bubbles. This becomes even more challenging with increasing surfactant concentration as the CGA becomes more stable and large bubbles tend to rise to the surface and hide the smaller ones.

Moreover, the CGA stability increases significantly with surfactant concentration. For example, CGA generated with 2.17 wt.% of Tween 20 or more is very stable and "creamy" while that generated

Table 1
Characteristics of the different Tween 20 solutions used in this study

Solution	Concentration (mM)	Mass fraction, x (wt.%)	pH	Surface tension, σ (mN/m)	Average porosity, ϕ	Sauter radius, r_{32} (μm)
1	0.21	0.028	4.85 ± 0.09	41.2 ± 1.14	0.63	47.6
2	1.71	0.22	4.53 ± 0.11	41.5 ± 1.0	0.68	41.9
3	4.26	0.55	4.24 ± 0.09	39.0 ± 1.0	0.71	36.8
4	16.77	2.17	3.94 ± 0.03	38.8 ± 0.6	0.72	40.8
5	32.90	4.23	3.76 ± 0.11	38.4 ± 1.54	0.71	39.4
6	77.77	9.96	4.28 ± 0.03	38.9 ± 1.54	0.70	39.0

Tween 20: $\rho = 1050\ kg/m^3$ and $M = 1.227\ kg/mol$.

using 0.028 wt.% is much less stable. The relatively small differences in bubble radius can be attributed to the fact that the surface tension – which varies slightly with the mass fractions considered – is the controlling parameter of the bubble diameter. This is also apparent in the average porosity which increases from 0.63 with 0.028 wt.% of Tween 20 to 0.70–0.72 beyond 0.55 wt.%. In all cases, it was verified that no appreciable changes can be observed in both the porosity and the bubble size distribution as CGA flows through the minichannels except for the 3 mm diameter pipe. Indeed, micrographs of CGA taken at the inlet and outlet of the 3 mm pipe indicate that the Sauter mean radius increases from 32 to 86 μm while the bubble size distribution widens as the CGA flows through the 3 mm in diameter and 1.03 m long pipe. This was not observed for smaller and shorter pipes.

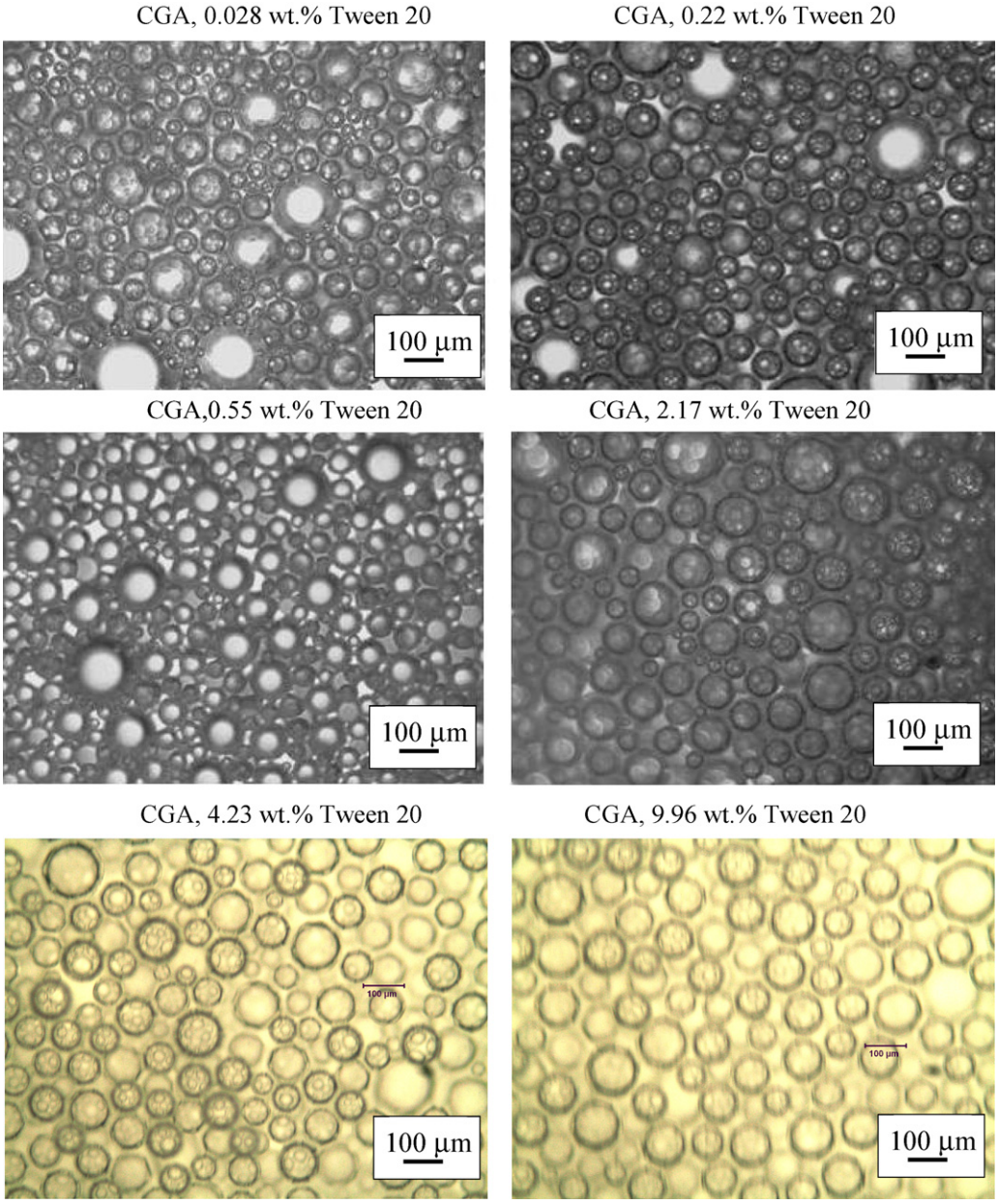

Fig. 3. Typical micrograph of CGA formed with different aqueous solution at 25 ± 2 °C.

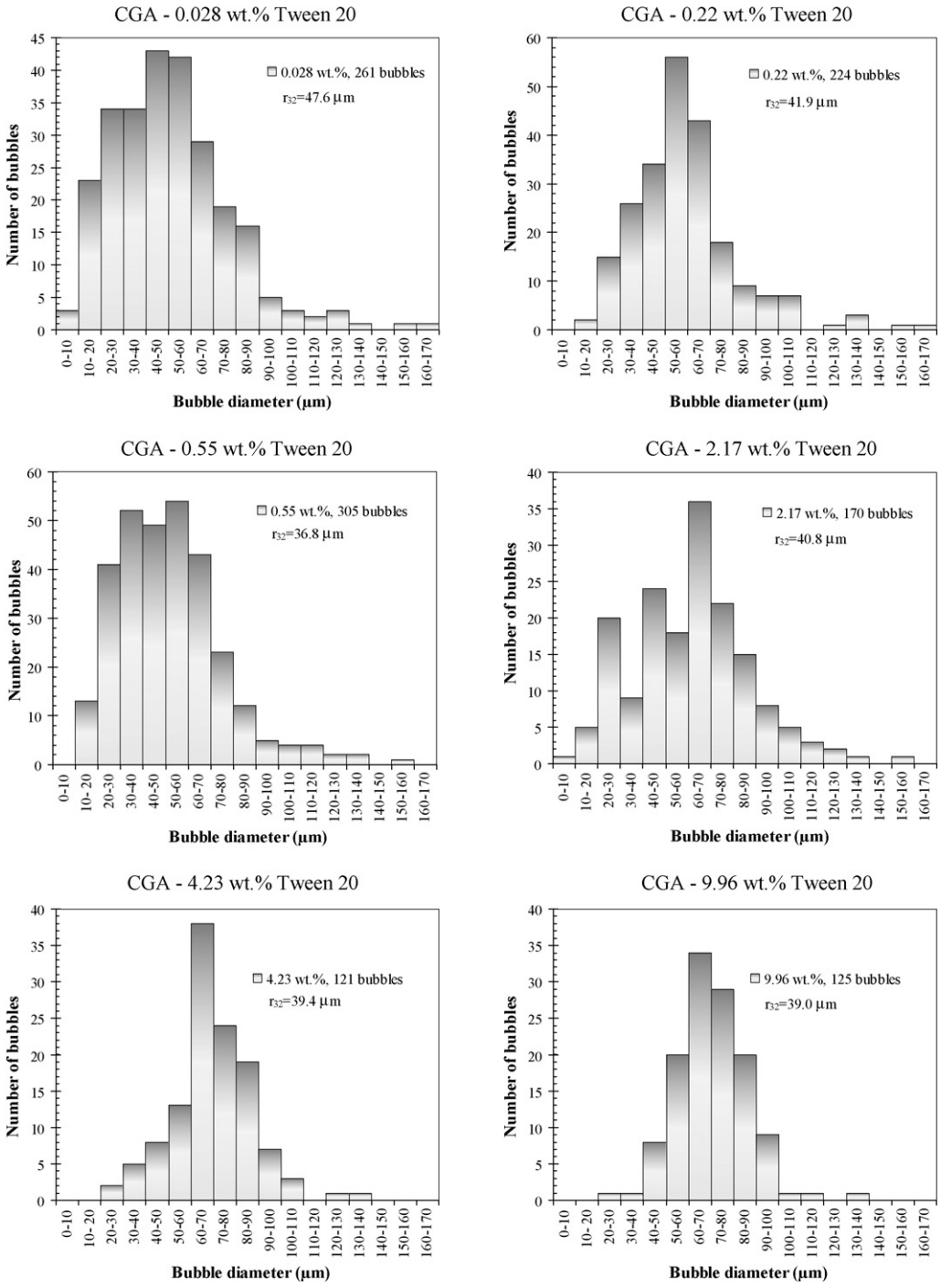

Fig. 4. Bubble size distribution of CGA formed with different aqueous solution at 25 ± 2 °C.

Finally, the fact that the surface tension of the solutions against air did not vary significantly for concentrations of Tween 20 larger than 0.22 wt.% suggests that the critical micelle concentration is less than 0.22 wt.% as suggested also in the literature [55]. However, it remains unclear whether these micelles subsist in the liquid phase of the CGA or disperse due to the presence of a large air/liquid interfacial area.

4.3. Pressure drop

Fig. 5 shows the pressure drop per unit length of pipe $\Delta P/L$ corrected for minor losses for CGA made from an aqueous solution of Tween 20 at 0.22 wt.% (Solution 2) and flowing in minichannels with different pipe diameters and cross-sections. The minor losses were computed from Eqs. (11) and (12) using the density of CGA defined as $\rho_{CGA} = M_{CGA}(t)/V_{CGA}(t)$. As expected, the pressure drop for CGA increased with decreasing pipe diameter. In addition, the pressure drop measured for the rectangular minichannel of cross-section 0.762 mm × 1.58 mm [45] was much smaller than that for the cylindrical pipe with identical hydraulic diameter of 1.03 mm, CGA porosity, Tween 20 concentration, channel length L, and temperature. This can be attributed to the fact that ΔP is inversely proportional to the cross-sectional area of the channel which is seven times larger for the rectangular channel [45] than for

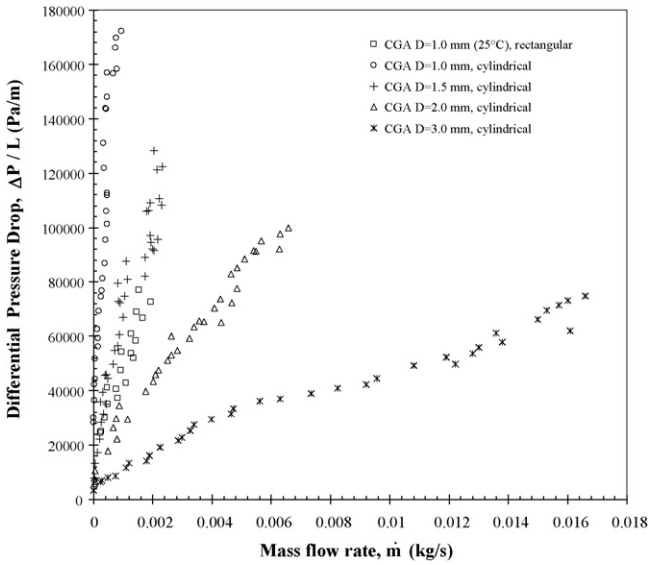

Fig. 5. Differential pressure drop ΔP [Eq. (11)] vs. mass flow rate $\dot{m}$ for CGA made of 0.22 wt.% aqueous solution of Tween 20 and for various pipe diameters at 25 ± 2 °C.

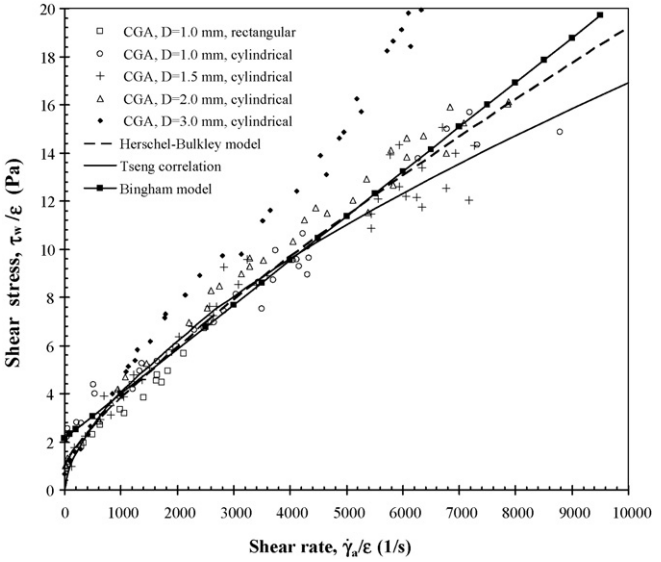

Fig. 7. Volume equalized shear stress vs. shear rate for CGA in pipes with various diameters. CGA is made of 0.22 wt.% aqueous Tween 20 solution at 25 ± 2 °C.

the cylindrical pipes with the same hydraulic diameter of 1.03 mm. Note that measurements reported in the present study are highly repeatable.

4.4. Rheology

Fig. 6 shows the shear stress versus apparent shear rate for CGA made with Solution 2 (x = 0.22 wt.%) flowing in 1.03, 1.49, 2.02, and 3.0 mm cylindrical pipes as well as in rectangular channels of hydraulic diameter 1.03 mm [45]. First, the data for cylindrical pipes was analyzed for the wall slip velocity. The apparent shear rate $\dot{\gamma}_a$ was found to be independent of $1/D_h$ (Mooney's model) and of $1/D_h^2$ (Oldroyd–Jastrzebski's model) for any arbitrary value of τ_w. Thus, no wall slip velocity was observed, in agreement with observations of aqueous foams flowing through stainless steel pipes [23,47]. Fig. 6 also suggests that the shape of the pipe has no effect

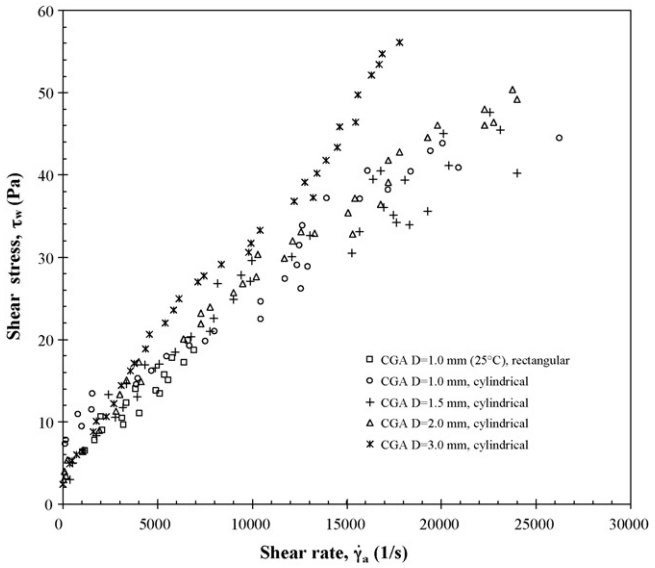

Fig. 6. Shear stress vs. shear rate for CGA in cylindrical and rectangular channels of various hydraulic diameters. CGA is made of 0.22 wt.% aqueous solution of Tween 20 at 25 ± 2 °C.

on the CGA rheology since data reported by Tseng and Pilon [45] for rectangular minichannels overlap with those for cylindrical pipes having the same hydraulic diameter of 1.03 mm.

To account for compressibility effects, the volume equalized shear stress τ_w/ε is plotted versus the volume equalized apparent shear rate $\dot{\gamma}_a/\varepsilon$ as shown in Fig. 7. Then, the data for pipe diameters 1.03, 1.49, and 2.02 mm are similar and collapse on the same line. However, shear stress measured for the 3 mm cylindrical pipe was larger than for the other pipes at the same shear stress. These discrepancies can be attributed to the change in the bubble size distribution observed between the inlet and outlet of the 3 mm pipe. Indeed, to ensure fully developed laminar flow, the 3 mm pipe is longer than the others. Thus, for a given shear rate, the residence time of CGA in the 3 mm pipe is larger and bubble coalescence is more likely to occur causing the average bubble diameter to increase particularly for low surfactant concentrations. For example, the average diameter varies from 31.8 μm at the inlet to 86.0 μm at the outlet of the 3 mm diameter pipe for CGA made from Solution 2. In addition, the pressure gradient may no longer be constant and the analysis may not apply. Thus, data from the 3 mm diameter pipe were not considered further. Therefore, Fig. 7 establishes that, after accounting for compressibility effects through the volume equalization approach [19–21], the pipe diameter has practically no effect on the CGA rheology. This is provided that the CGA bubble size distribution does not change between the inlet and outlet of the pipe. Note also that the geometry independence of the volume equalized power-law model was also established for polymer foams [19–21].

Furthermore, Figs. 6 and 7 also indicate that CGA can be classified as a shear-thinning fluid, a Bingham fluid, or Hershel–Bulkley fluid. Curve fitting the data obtained for each pipe individually gives similar values for the power index, consistency and yield shear stress and are in good agreement with those obtained by Tseng and Pilon [45] for rectangular channels. The correlations between the volume equalized apparent shear rate and shear stress obtained by least-square curve fitting of all experimental data for CGA made of 0.22 wt.% aqueous solution of Tween 20 flowing in cylindrical pipes and rectangular minichannels are given, respectively, by

$$\frac{\tau_w}{\varepsilon} = 0.04\left(\frac{\dot{\gamma}_a}{\varepsilon}\right)^{0.62}, \qquad \frac{\tau_w}{\varepsilon} = 2.145 + 1.85 \times 10^{-3}\left(\frac{\dot{\gamma}_a}{\varepsilon}\right), \quad \text{and}$$

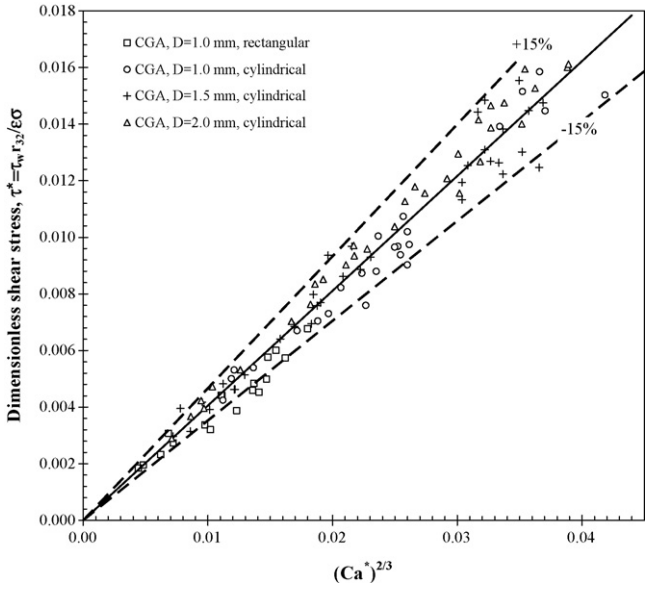

Fig. 8. Dimensionless volume equalized shear stress vs. $(Ca^*)^{2/3}$ for CGA in various diameter pipes. CGA is made of 0.22 wt.% aqueous Tween 20 solution at 25 ± 2 °C.

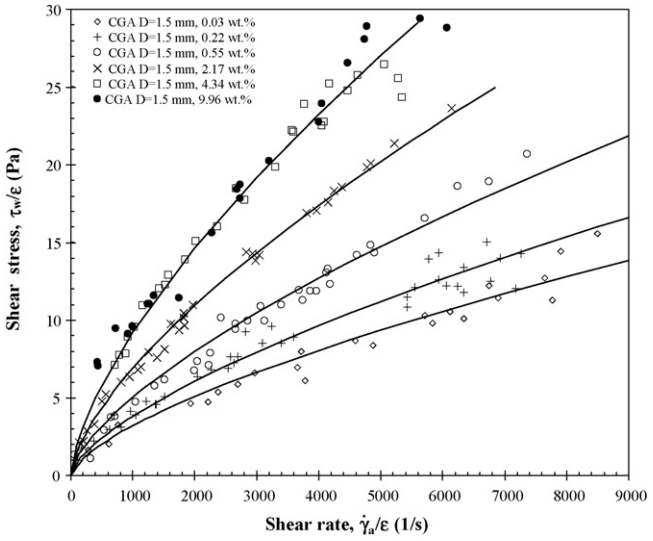

Fig. 9. Volume equalized shear stress vs. shear rate for CGA made from aqueous solution of Tween 20 with different mass fractions obtained in the 1.5 mm diameter pipe at 25 ± 2 °C.

$$\frac{\tau_w}{\varepsilon} = 1.2 + 1.1 \times 10^{-2} \left(\frac{\dot{\gamma}_a}{\varepsilon}\right)^{0.8} \quad (16)$$

The *R*-squared values associated with the above correlations are larger than 0.95 and can be considered equivalent for all practical purposes. Indeed, predictions of the above Bingham model and the Herschel–Bulkley model fall within 11% of the power-law model for apparent shear rate between 1000 and 10,000 s^{-1}. Below apparent shear rate of 1000 s^{-1}, experimental uncertainties on τ_w and $\dot{\gamma}_a$ are large and yield stress is difficult to estimate as also reported by Enzendorfer et al. [20] and Herzhaft [18]. Thus, the power-law model is recommended by virtue of its simplicity and its physical relevance and in agreement with previous studies on CGA and macrofoams.

To make the results more general, the volume equalized apparent shear rate and shear stress are non-dimensionalized in terms of Capillary number Ca^* and dimensionless stress τ^* expressed, respectively, as

$$\tau^* = \frac{\tau_w r_{32}}{\sigma\varepsilon} \quad \text{and} \quad Ca^* = \frac{\mu_l r_{32} \dot{\gamma}_a}{\varepsilon\sigma} \quad (17)$$

Fig. 8 shows τ^* versus $(Ca^*)^{2/3}$ for pipe diameters 2 mm or less and surfactant mass fraction of 0.22 wt.%. It establishes that $\tau^* = 0.36(Ca^*)^{2/3}$. This agrees with the theoretical models [34,35] assuming mobile bubble surface and suggests that the shear stress is dominated by friction in the meniscus region of the bubbles. Note also that the surface dilatational modulus of aqueous Tween 20 in air is relatively small and of the order of 20 mN/m at pH 5 and concentration of 10^{-4} to 0.05 M [56]. This suggests that the surface is tangentially mobile in agreement with experimental data reported by Denkov et al. [35].

Finally, the present study suggests that discrepancies among previous studies on foams could have been caused not only by compressibility effects [17,19–21] and wall slip velocity [19–21] but also by changes in the foam morphology during the measurements.

4.5. Effect of surfactant concentration

The effect of surfactant concentration on rheological properties of foams and CGA has been considered in a few earlier studies [27,43,46,57]. They concluded that the pressure drop and the effective viscosity of wet foams flowing in a vertical pipe increased with surfactant concentration [27,46]. Similar results were observed for CGA flowing in horizontal and long capillaries [57].

In the present study, the effect of concentration of surfactant on CGA rheology was assessed with aqueous solutions of Tween 20 at mass fractions 0.028, 0.22, 0.55, 2.17, 4.23, and 9.96 wt.%. Fig. 9 shows the volume equalized shear stress τ_w/ε as a function of the volume equalized apparent shear rate $\dot{\gamma}_a/\varepsilon$ for these four surfactant solutions flowing through the cylindrical pipe 1.5 mm in diameter. First, it indicates that experimental data points become less scattered and more consistent as the surfactant concentration increases thanks to the increased stability of the CGA. Fig. 9 also establishes that τ_w/ε increases significantly with surfactant concentration for a given value of $\dot{\gamma}_a/\varepsilon$. This was also observed by Oliveira et al. [57]. This cannot be attributed to changes in surface tension since it does not vary significantly over the range of surfactant mass fractions considered (Table 1). Similarly, porosity remains constant at 0.70–0.72 for concentrations larger than 0.55 wt.% while the shear stress versus apparent shear rate curves differ significantly.

The increase in τ_w/ε with surfactant concentration at a given value of $\dot{\gamma}_a/\varepsilon$ could be attributed to the reduction in the maximum packing of spherical bubbles as their size distribution narrows (see Fig. 4). Indeed, it has been established that the maximum packing of spherical solid particles is larger for polydisperse systems than for their monodisperse counterpart with the same volume fraction [58]. As the maximum packing decreases so does the viscosity [58]. In addition, if one accepts the shell structure of CGA bubbles proposed by Sebba [1], the shell may become thicker with increasing surfactant concentration. Thus, the bubble interfaces become "stiffer" and bubbles behave more like solid particles while maintaining tangentially mobile surface. This would result in an increase in pressure drop and shear stress [59]. The increase in shear stress could also be caused by an increase in the viscosity of the surfactant solution itself or by the presence of micelles in the liquid phase. However, pipe flow measurements suggests that the aqueous solution of Tween 20 with mass fraction of 2.17 and 4.23 wt.% behaves as a Newtonian fluid with the same viscosity as deionized water as shown in Fig. 2. Thus, the potential presence of micelles in the liquid phase cannot explain the increase in shear stress with surfactant concentration for a given apparent shear rate. The viscosity of the surfactant solution of mass fraction 9.96 wt.% increases to

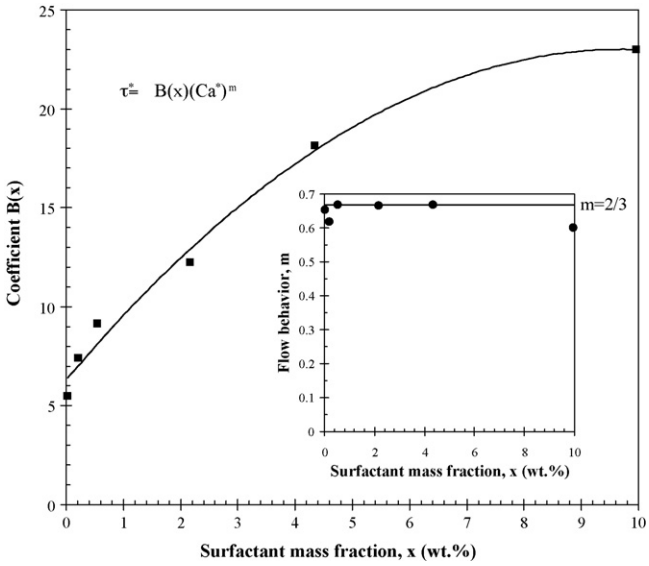

Fig. 10. Empirical coefficient $B(x)$ and power index m in Eq. (18) as a function of Tween 20 mass fraction obtained in the 1.5 mm diameter pipe at 25 ± 2 °C.

1.87 mPa s (Fig. 2) due most likely to the presence of micelles. It remains unclear however, whether these micelles still exist in the liquid phase once the microfoam is formed and if the viscosity of the liquid phase in the microfoam is the same as that of the single-phase Tween 20 solution.

Moreover, Fig. 9 suggests that the CGA can be considered as a shear-thinning fluid in terms of volume equalized apparent shear rate and shear stress with empirical constants dependent on surfactant concentration. The data shown in Fig. 9 can be fitted using the power law:

$$\tau^* = B(x)(Ca^*)^m \tag{18}$$

Fig. 10 shows the evolution of the empirical coefficient $B(x)$ and the power index m as a function of surfactant mass fraction x. It indicates that the average value of the power index m is 0.65 ± 0.06 while $B(x)$ increases quadratically with surfactant mass fraction according to $B(x) = 6.30 + 3.46x - 0.18x^2$ for 0.028 wt.% ≤ x ≤ 9.96 wt.%.

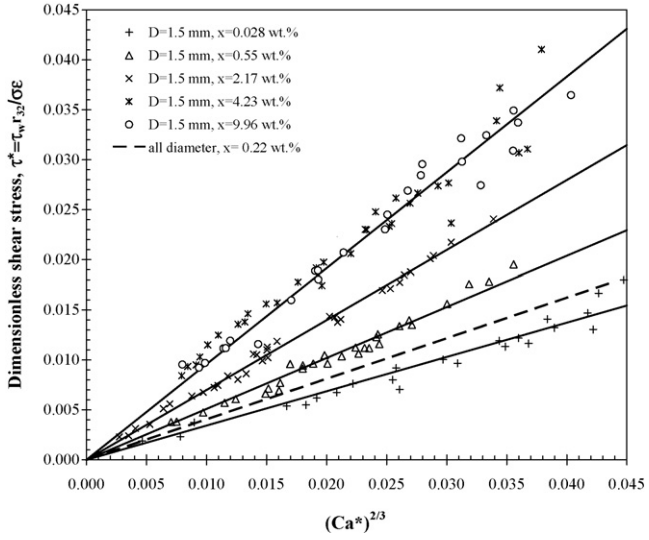

Fig. 11. Volume equalized dimensionless shear stress vs. $(Ca^*)^{2/3}$ for CGA made from aqueous solution of Tween 20 with different mass fraction obtained in the 1.5 mm diameter pipe at 25 ± 2 °C.

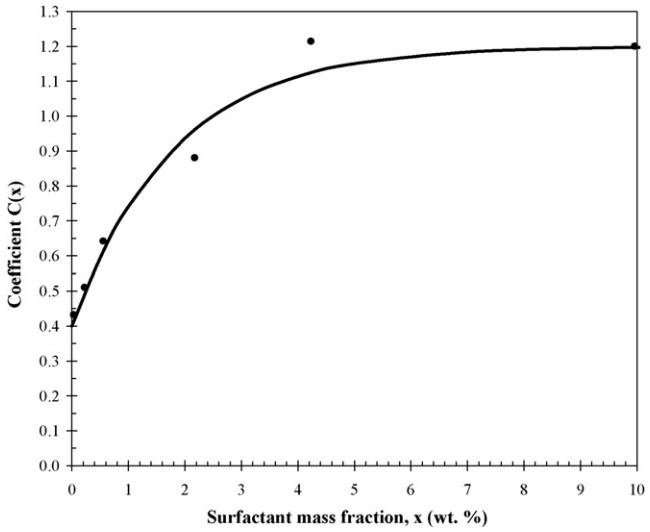

Fig. 12. Empirical constant $C(x)$ in Eq. (19) as a function of Tween 20 mass fraction obtained in the 1.5 mm diameter pipe at 25 ± 2 °C.

The results were also plotted in Fig. 11 in terms of dimensionless shear stress τ^* as a function of volume equalized Capillary number $(Ca^*)^{2/3}$ and show a linear relationship expressed as

$$\tau^* = C(x)(Ca^*)^{2/3} \quad \text{with} \quad C(x) = 0.4 + 0.8(1 - e^{-x/0.018}) \tag{19}$$

For the sake of completeness, Fig. 12 shows the evolution of parameter $C(x)$ as a function of mass fraction x. It is evident that beyond a surfactant mass fraction of 0.0423, $C(x)$ no longer depends on surfactant concentration and reaches a constant value of 1.2. Note that the constant $C(x)$ was not expressed in terms of porosity due to the small range of values explored and the associated experimental uncertainty.

4.6. Friction factor

For engineering applications, it is often convenient to express rheology data of fluids in terms of Fanning friction factor as a func-

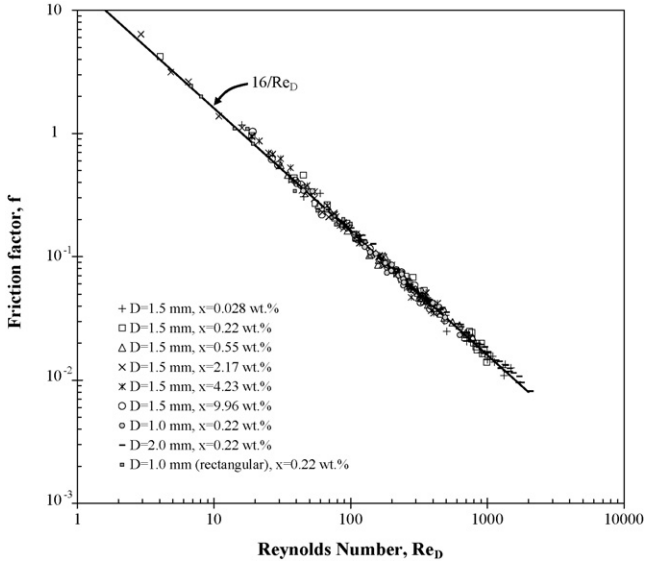

Fig. 13. Fanning friction factor vs. Reynolds number for various pipe diameters and Tween 20 mass fractions.

tion of Reynolds number to estimate the pressure drop. The Fanning friction factor and the Reynolds number are defined as

$$f = \frac{\tau_w}{\rho_f u_f^2/2} \quad \text{and} \quad Re_D = \frac{\dot{m} D_h}{\mu_e} \tag{20}$$

where μ_e is the fluid effective dynamic viscosity derived from Eqs. (1) and (19) as

$$\mu_e = C(x)\mu_l (Ca^*)^{-1/3} \tag{21}$$

Fig. 13 shows the friction factor f versus Reynolds number Re_D for all the experimental data collected. It shows that the friction factor follows the well-known correlation $f = 16/Re_D$ for laminar flows.

5. Conclusions

The present study focused on the effects of the pipe shape and hydraulic diameters and of the surfactant concentration on the rheology of colloidal gas aphrons. The following conclusions can be drawn from the experimental data:

1. No slip velocity was observed in agreement with other experiments for aqueous foam rheology in stainless steel pipes [47].
2. The CGA rheology is not affected by the pipe shape or hydraulic diameter provided that the bubble size distribution does not change during the measurements.
3. The CGA can be treated as a shear-thinning fluid. The dimensionless volume equalized shear stress τ^* is proportional to the Capillary number Ca^* raised to power $m = 0.65 \pm 0.06$ in agreement with theoretical model for bubbles with tangentially mobile surfaces which suggests that $m = 2/3$.
4. Increasing the surfactant concentration causes the shear stress to increase for a given apparent shear rate. This could be attributed to (i) the decrease in the maximum packing due to narrower size distribution or to (ii) the possible increase in the thickness of the surfactant shell surrounding the CGA bubbles making them less deformable and behave as solid spheres.
5. The friction factor follows the standard $16/Re_D$ where the Reynolds number is estimated with the effective viscosity of CGA given by $\mu_e = C(x)\mu_l (Ca^*)^{-1/3}$.

Future studies should consider surfactants with different molecule size, ionicity, and critical micelle concentration, for example. The structure of the CGA bubbles and the presence and nature of the suspected shell should also be explored in details as it may affect the CGAs rheological properties.

Acknowledgements

Acknowledgment is made to the Donors of the American Chemical Society Petroleum Research Fund for partial support of this research. The authors are indebted to the anonymous referees whose comments helped improve the final manuscript. They would also like to thank Prof. Brent W. Webb for useful discussion and exchange of information.

References

[1] F. Sebba, Foams and Biliquid Foams—Aphrons, John Wiley & Sons, New York, 1987.
[2] G. Spigno, P. Jauregi, Recovery of Gallic acid with colloidal gas aphrons (CGA), Int. J. Food Eng. 1 (4) (2005), article no. 5.
[3] P. Jauregi, J. Varley, Colloidal gas aphrons: a novel approach to protein recovery, Biotechnol. Bioeng. 59 (1998) 471–481.
[4] D. Roy, K.T. Valsaraj, W.D. Constant, M. Darji, Removal of hazardous oily waste from a soil matrix using surfactants and colloidal gas aphron suspensions under different flow conditions, J. Hazard. Mater. 38 (1994) 127–144.
[5] D. Roy, R.R. Kommalapati, K.T. Valsaraj, W.D. Constant, Soil flushing of residual transmission fluid: application of colloidal gas aphron suspensions and conventional surfactant solutions, Water Res. 29 (1995) 589–595.
[6] R.W. Grimes, Evaluation of a method using colloidal gas aphrons to remediate metals contaminated mine drainage waters, Western Research Institute Report WRI-02-R007, 2002.
[7] S. Ciriello, S.M. Barnett, F.J. Deluise, Removal of heavy-metals from aqueous-solutions using microgas dispersions, Sep. Sci. Technol. 4 (1982) 521–534.
[8] J. Weber, F.A. Agblevor, Microbubble fermentation of *Trichoderma reesei* for cellulase production, Process Biochem. 40 (2) (2005) 669–676.
[9] A.E. Riviello, D. Young, F. Sebba, A novel method for production of finely divided tin metal powders, Powder Technol. 78 (1994) 19–24.
[10] R.J. Davey, H. Alison, J.J. Cilliers, J. Garside, A new strategy for preparing macroporous materials: using a colloidal gas aphron to create an oriented crystal network, Chem. Commun. 23 (1998) 2581–2582.
[11] S.F. Abdullah, S. Radiman, M.A.Abd. Hamid, N.B. Ibrahim, Effect of calcination temperature on the surface morphology and crystallinity of tungsten (VI) oxide nanorods prepared using colloidal gas aphrons method, Colloids Surf. A: Physicochem. Eng. Aspects 280 (1–3) (2006) 88–94.
[12] M.D. Bredwell, R.M. Worden, Mass transfer properties of microbubbles. 1. Experimental studies, Biotechnol. Prog. 14 (1998) 31–38.
[13] D. Weaire, S. Hutzler, The Physics of Foams, Oxford University Press, USA, 2001.
[14] R. Höhler, S. Cohen-Addad, Rheology of liquid foams, J. Phys.: Condens. Matter 17 (2005) R1041–R1069.
[15] P. Jauregi, G.R. Mitchell, J. Varley, Colloidal gas aphrons (CGA): dispersion and structural features, Am. Inst. Chem. Eng. J. 46 (2000) 24–36.
[16] M.C. Amiri, E.T. Woodburn, A method for the characterization of colloidal gas aphron dispersions, Chem. Eng. Res. Des. 68 (1990) 154–160.
[17] J.P. Heller, M.S. Kuntamukkula, Critical review of the foam rheology literature, Ind. Eng. Chem. Res. 26 (2) (1987) 318–325.
[18] B. Herzhaft, Rheology of aqueous foams: a literature review of some experimental works, Oil Gas Sci. Technol. Revue del'IFP 54 (5) (1999) 587–596.
[19] P. Valko, M.J. Economides, Volume equalized constitutive equations for foamed polymer solutions, J. Rheol. 36 (1992) 111–127.
[20] C. Enzendorfer, R.A. Harris, P. Valko, M.J. Economides, P.A. Fokker, D.D. Davies, Pipe viscometry of foams, J. Rheol. 39 (2) (1995) 345–356.
[21] W. Winkler, P. Valko, M.J. Econmides, Laminar and drag-reduced polymeric foam flow, J. Rheol. 38 (1) (1994) 111–127.
[22] J.T. Patton, H. Belkin, S. Holbrook, M. Kuntamukkula, Rheology of mobility-control foams, Soc. Petrol. Eng. J. 23 (1983) 456–460.
[23] N.N. Thondavali, R. Lemlich, Flow properties of foam with and without solid particles, Ind. Eng. Chem. Process Des. Dev. 24 (1988) 748–753.
[24] V. Sanghani, C.U. Ikoku, Rheology of foam and its implications in drilling and cleanout operations, ASME J. Energy Resour. Technol. 105 (3) (1983) 362–371.
[25] F.A. Morrison, Understanding Rheology, Oxford University Press, Oxford, UK, 2001.
[26] S.A. Khan, C.A. Schnepper, R.C. Amstrong, Foam rheology. III. Measurement of shear flow properties, J. Rheol. 32 (1) (1988) 69–92.
[27] B. Herzhaft, S. Kakadjian, M. Moan, Measurement and modeling of the flow behavior of aqueous foams using a recirculating pipe rheometer, Colloids Surf. A: Physicochem. Eng. Aspects 263 (2005) 153–164.
[28] S.A. Khan, R.C. Amstrong, Foam rheology. I. Theory for dry foams, J. Non-Newton. Fluid Mech. 22 (1) (1987) 1–22.
[29] A.M. Kraynick, M.G. Hansen, Foam rheology: a model of viscous phenomena, J. Rheol. 31 (1987) 175–205.
[30] H.M. Princen, A.D. Kiss, Rheology of foams and highly concentrated emulsions. IV. An experimental study of shear viscosity and yield stress of concentrated emulsions, J. Colloidal Interface Sci. 128 (1989) 176–187.
[31] L.W. Schwartz, H.M. Princen, A theory of extensional viscosity for flowing foams and concentrated emulsion, J. Colloidal Interface Sci. 118 (1) (1987) 201–211.
[32] F.P. Bretherton, The motion of long bubbles in tubes, J. Fluid Mech. 10 (1961) 166–188.
[33] A.M. Kraynick, Foam flows, Annu. Rev. Fluid Mech. 20 (1988) 325–327.
[34] N.D. Denkov, V. Subramanian, D. Gurovich, A. Lips, Wall slip and viscous dissipation in sheared foams: effect of surface mobility, Colloids Surf. A: Physicochem. Eng. Aspects 263 (2005) 129–145.
[35] N.D. Denkov, S. Tcholakova, K. Golemanov, V. Subramanian, A. Lips, Foam–wall friction: effect of air volume fraction for tangentially immobile bubble surface, Colloids Surf. A: Physicochem. Eng. Aspects 282/283 (2006) 329–347.
[36] I. Cantat, N. Kern, R. Delannay, Dissipation in foam flowing through narrow channels, Europhys. Lett. 65 (5) (2004) 726–732.
[37] E. Terriac, J. Etrillard, I. Cantat, Viscous force exerted on a foam at a solid boundary: influence of the liquid fraction and of the bubble size, Europhys. Lett. 74 (5) (2006) 909–915.
[38] D.J. Durian, Foam mechanics at the bubble scale, Phys. Rev. Lett. 75 (26) (1995) 4780–4783.
[39] D.J. Durian, Bubble-scale model of foam mechanics: melting, nonlinear behavior, and avalanches, Phys. Rev. E 55 (2) (1997) 1739–1751.
[40] B.S. Gardiner, B.Z. Dlugogorski, G.J. Jameson, The steady shear of three-dimensional wet polydispersed foams, J. Non-Newton. Fluid Mech. 92 (2000) 151–166.
[41] J.R. Calvert, K. Nezhati, A rheological model for a liquid–gas foam, Int. J. Heat Fluid Flow 7 (1985) 164–168.

[42] S.H. Raza, S.S. Marsden, The streaming potential and the rheology of foams, Soc. Petrol. Eng. J. 7 (1967) 359–363.
[43] N.S. Deshpande, M. Barigou, The flow of gas–liquid foams in vertical pipes, Chem. Eng. Sci. 55 (2000) 4297–4309.
[44] B.S. Gardiner, B.Z. Dlugogorski, G.J. Jameson, Rheology of fire-fighting foams, Fire Saf. J. 31 (1998) 61–75.
[45] H. Tseng, L. Pilon, Rheology and convective heat transfer properties of colloidal gas aphrons in horizontal minichannels, Int. J. Heat Fluid Flow 27 (2) (2006) 298–310.
[46] R.K. Prud'homme, S.A. Khan, Experimental results on foam rheology in foams: theory, measurements, and applications, in: R.K. Prud'homme, S.A. Khan (Eds.), Surfactant Science Series, vol. 57, Marcel Dekker, New York, NY, 1996, pp. 217–242.
[47] P.C. Harris, V.G. Reidenbach, High-temperature rheological study of foam facturing fluids, J. Petrol. Technol. 39 (5) (1987) 613–619.
[48] N. Mooney, Explicit formulas for slip and fluidity, J. Rheol. 2 (1931) 210–222.
[49] J.G. Oldroyd, The interpretation of observed pressure gradients in laminar flow of non-Newtonian liquids through tubes, J. Colloid Sci. 4 (3) (1949) 333–342.
[50] Z.D. Jastrzebski, Entrance effects and wall effects in an extrusion rheometer during flow concentrated suspensions, Ind. Eng. Chem. Fundam. 6 (3) (1967) 455.
[51] Y.A. Çengel, J.M. Cimbala, Fluid Mechanics: Fundamentals and Applications, 1st edition, McGraw-Hill, New York, NY, 2004.
[52] M.I. Briceño, D.D. Joseph, Self-lubricated transport of aqueous foams in horizontal conduits, Int. J. Multiphase Flow 29 (2003) 1817–1831.
[53] Thermophysical Properties Database DIPPR 801, http://dippr.byu.edu/database.asp.
[54] D.R. Lire (Ed.), CRC Handbook of Chemistry and Physics, Internet Version 2007, 87th edition, Taylor and Francis, Boca Raton, FL, 2006–2007 http:/www.hbcpnetbase.com.
[55] S.C. Kothekar, A.M. Ware, J.T. Waghmare, S.A. Momin, Comparative analysis of the properties of Tween-20, Tween-60, Tween-80, Arlacel-60, and Arlacel-80, J. Dispers. Sci. Technol. 28 (2007) 477–484.
[56] V.P. Ruiz Henestrosa, C. Carrera Sanchez, J.M. Rodriguez Patino, Formulation engineering can improve the interfacial and foaming properties of soy globulins, J. Agric. Food Chem. 55 (2007) 6339–6348.
[57] R.C.G. Oliveira, J.F. Oliveira, B.M. Moudgil, Optimizing micro-foam rheology for soil remediation, Prog. Colloid Polym. Sci. 128 (2004) 298–302.
[58] J.J. Stickel, R.L. Powell, Fluid mechanics and rheology of dense suspensions, Annu. Rev. Fluid Mech. 37 (2005) 129–149.
[59] M. Ishii, N. Zuber, Drag coefficient and relative velocity in bubbly, droplet, or particulate flows, AIChE J. 25 (5) (1979) 843–855.